Available online at www.sciencedirect.com
SCIENCE DIRECT®
Journal of Nuclear Materials 322 (2003) 126–137
journal of nuclear materials
www.elsevier.com/locate/jnucmat

The mechanical testing of nuclear graphite

B.C. Mitchell, J. Smart *, S.L. Fok, B.J. Marsden

Manchester School of Engineering, University of Manchester, Oxford road, Manchester M13 9PL, UK

Received 2 February 2003; accepted 24 June 2003

Abstract

Two billets of nuclear grade medium-grained semi-isotropic graphite were machined into rectangular 4-point bend and L-shaped specimens and tested to failure. The material was not irradiated. During the testing, as well as determining the failure load, the failure was monitored by a high speed camera. The results showed that: there was a difference in the failure loads both along a billet and between the billets, in the L-shaped specimens the cracks did not fail instantaneously but needed further movement of the testing machine's crosshead before total failure, and the speed of the crack varied in the different specimens. The data were analysed and it was found that the Weibull theory does not predict the failure well but fracture mechanics does provide a way of correlating the data, particularly the crack propagation.

1. Introduction

In a graphite moderated nuclear reactor such as Magnox, AGR and HTR, the integrity of the graphite core is one of the factors that determine its life. However, whilst the failure of metals can be reasonably well predicted, the failure of brittle materials in general, and graphite in particular, cannot be well characterised [1]. In addition, when irradiated properties change due to fast neutron damage and oxidation these effects will also need to be accounted for. By testing virgin graphite it is hoped to obtain a deeper understanding which will give confidence in examining the irradiated data that are already available and new irradiation data being obtained at present from graphite reactor monitoring campaigns and material test reactor programmes. Consequently, this paper presents the results of testing of graphite in two configurations and attempts to correlate the data.

Two billets of PPEA graphite supplied by UCAR/GrafTech were tested. PPEA is a high quality, very pure extruded medium-grained graphite which is used to manufacture nuclear reactor components and has a grain size of 0.36–0.76 mm and a density of 1.85 g/cm^3. It is manufactured by extrusion which tends to align the crystal graphite structure preferentially in the direction of extrusion giving an isotropy factor, as defined by coefficient of thermal expansion, of 1.07. Similarly, other properties such as strength and modulus tend to be different 'with the grain' (the extrusion direction) and 'perpendicular to the grain'. It should also be noted that during manufacture, there are other effects that may influence the graphite billet variability.

The billets were machined into 4-point bend specimens and also into L-shaped specimens with varying corner radii. The 4-point bend specimens were used to characterise the material. Within a billet, the 4-point specimens were machined at three orientations to the axis of the billet and from both ends; these tests were chosen to show if there was any variation of properties around the billet, along the billet and from billet to billet. As with any brittle material, there is a considerable scatter of failure loads and many specimens are necessary to characterise the failure. The failure is often characterised using Weibull statistics and typically about 30 specimens are tested. In a recent paper [2] the present authors have examined the number of specimens needed to determine the Weibull parameters and shown that

* Corresponding author. Tel.: +44-161 275 4350; fax: +44-161 275 3844.
E-mail address: john.smart@man.ac.uk (J. Smart).

0022-3115/$ - see front matter © 2003 Elsevier B.V. All rights reserved.
doi:10.1016/S0022-3115(03)00322-2

this will depend on the threshold stress. However, in the present case the practicalities of testing have restricted the number of specimens although 96 4-point bend test specimens were tested from a single billet.

The L-shaped specimens were tested to examine the effect on the failure load of the radius in the corner and also the variation of failure load with specimen thickness. The corner was subjected to a tensile stress; this is similar to the load in a typical graphite moderated reactor component keyway root. The results were also used to examine whether the Weibull theory can be used to model the failure using material parameters from the 4-point bend tests. Further, the thickness of the L-shaped specimens was varied to try to detect if there is any effect from the surface-to-volume ratio. This is because in the analysis of the failure loads using Weibull theory, failure is assumed to arise from either surface or volume flaws. As the surface-to-volume ratio is varied, then the effects of different flaw populations may be found.

2. Experimental procedure

2.1. Sample preparation

The 4-point specimens were cut from the ends of the billets whilst the L-shaped specimens were cut from the centre of the billet. The cutting pattern is shown in Fig. 1 and the cutting schedule is given in Table 1 (where t is the specimen thickness and r the corner radius). The 4-point bend specimens had a width of 10 mm and a depth of 15 mm. The discs labelled D where machined into L-shaped specimens and the dimensions of the L-shaped specimens are given in Fig. 2. All the specimens were machined to a tolerance of 0.1 mm with a surface finish of 0.01 mm.

2.2. Specimen testing

The samples were all tested in a Schenck Universal testing machine at a constant crosshead displacement rate of 1 mm/min. For the L-shaped specimens the distance between the support points was 80 mm and the loading span was 20 mm. The specimens were loaded and supported on rollers. The L-shaped specimens were tested by placing a pin in each hole and attached to a loading rig and hence, the specimens subjected to a tensile load. In every test the load/displacement curve was plotted and the maximum failure load noted. For the 4-point bend tests, the specimens were measured to 0.01 mm and the failure loads converted to give the maximum stress in the specimens using the Engineer's bending theory. It is recognised that this will not be totally correct because the Engineer's bending theory is in error at the loading points [3,4], but no correction has

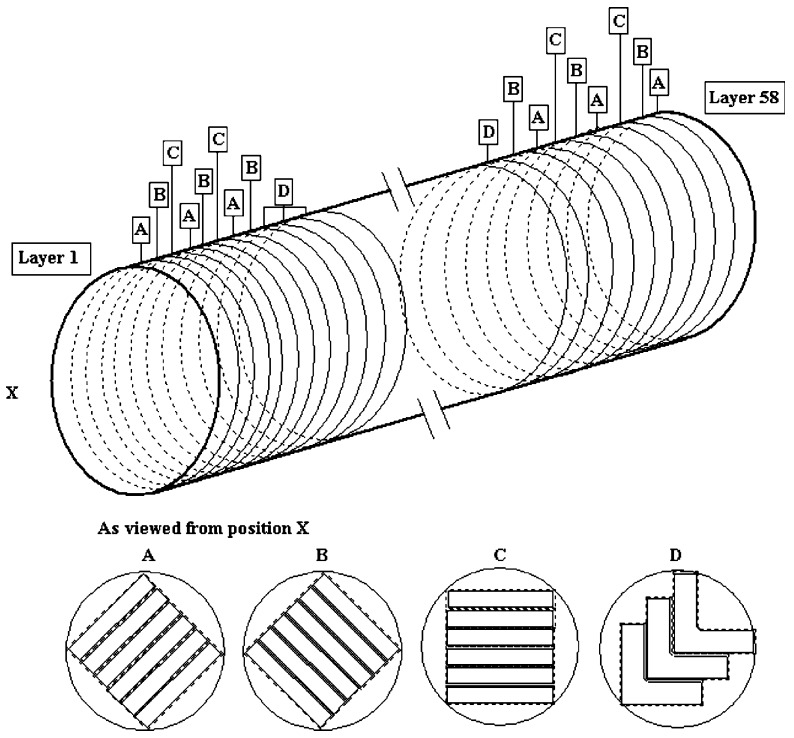

Fig. 1. Cutting pattern used in the manufacture of samples, not to scale.

Table 1
Cutting schedule for both billets

Layers	Sample description	Billet 1	Billet 2	Number of samples/billet
1, 4, 7	Beam	A	A	18
2, 5, 8	Beam	B	B	18
3, 6	Beam	C	C	12
9–22	L-specimen	$t = 10$, $r = 2$	$t = 15$, $r = 0$	42
23–36	L-specimen	$t = 15$, $r = 2$	$t = 15$, $r = 1$	42
37–50	L-specimen	$t = 20$, $r = 2$	$t = 15$, $r = 4$	42
51, 54, 57	Beam	B	B	18
52, 55, 58	Beam	A	A	18
53, 56	Beam	C	C	12

Dimensions in mm. For the L-shaped specimens t is the thickness and r is the corner radius – see Fig. 2.

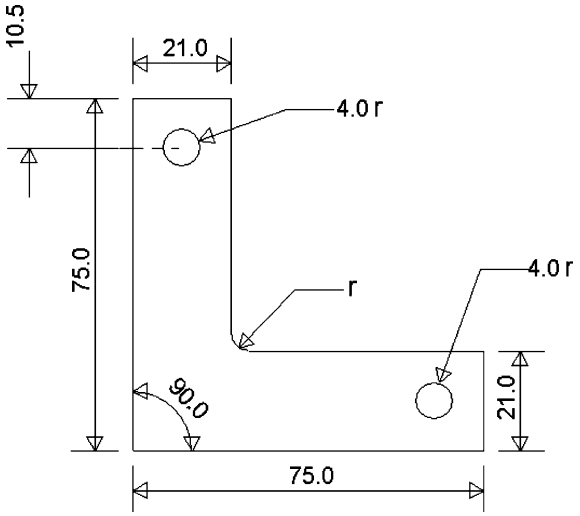

Fig. 2. Dimensions of L-shaped sample (in mm).

been made as it will only have a small effect on the results. It is recognised that although Refs. [3,4] are analyses for 3-point bending, similar effects are also present in 4-point bend specimens.

2.3. High speed filming

A high speed video camera was used to capture the failure in each configuration of graphite sample. Over 40 4-point bend specimens, and 9 samples from each L-shaped geometry were filmed using a Kodak HS4540 (obtained from the Engineering and Physical Sciences Research Council equipment loan pool), a digital camera capable of recording up to 40 500 frames per second (fps).

Difficulties were encountered in capturing the onset and propagation of cracking in the L-shaped specimens. Firstly, the frame rate of the camera had to be set at a low value (60–2500 fps) in order to gain sufficient footage time to capture the failure event as the camera could only hold 3072 frames and the camera was stopped manually. Secondly, when the cracks did form they were difficult to see, since the crack opening displacement was small. In addition, a crack in grey graphite is difficult to see. The samples were therefore sprayed with Ardrox HF-D, a spray used in crack detection, which was used to coat the samples with a white residue with no strength of its own. [1] Conventional acrylic paints were also tried but they formed an elastic 'skin' on the surface of the graphite which stretched as the specimen was strained, and hid the crack.

3. Results

3.1. Orientational anisotropy (perpendicular to direction of extrusion)

The mean failure stresses and Weibull moduli of the beam specimens in each orientation are summarised in Table 2. In this table 'top' refers to samples machined from layers 1–8, and 'bottom' refers to those originating from layers 51–58. There is no further implication in the use of these words. The Weibull modulus has been obtained using a two-parameter fit; i.e. assuming that the threshold stress is zero. The average of the 'top' and 'bottom' of the billets and the overall average for each billet are also summarised in Table 2 and these are discussed later.

It can be seen that there are differences in the properties in each of the three orientations at both ends of both billets. An important observation is that differences in mean failure stress and Weibull modulus observed at

[1] Ardrox HF-D is a non-chlorinated solvent based developer manufactured by Brent Europe Ltd. and is normally used in detecting cracks. It is an aerosol and leaves a very fine white deposit on the surface of the specimen.

Table 2
Comparison of orientational anisotropy in 4-point bend specimens from both ends of both billets, the average values for each end of each billet and the overall average for each billet

Orientation	Location	Billet	Mean σ_f (MPa)	Weibull modulus, m	No. of samples
A	Top	1	31.84	14.88	18
B	Top	1	33.81	12.14	18
C	Top	1	33.27	12.87	12
A	Bottom	1	31.49	13.91	18
B	Bottom	1	26.73	8.17	18
C	Bottom	1	30.42	14.15	12
A	Top	2	35.05	20.24	18
B	Top	2	33.35	9.50	18
C	Top	2	35.88	22.18	12
A	Bottom	2	33.65	12.95	18
B	Bottom	2	31.59	19.36	18
C	Bottom	2	32.97	21.94	12
	Top	1	32.93	13.33	48
	Bottom	1	29.44	9.19	48
	Top	2	34.62	12.99	48
	Bottom	2	32.71	15.80	48
	All	1	31.19	9.77	96
	All	2	33.67	14.00	96

one end of a billet are not duplicated at the other. For example, samples at the top of billet 1 in orientation A are slightly weaker than samples in orientations B and C at the top of that billet. However, at the bottom of the billet, samples in orientation A are slightly stronger than samples in the other two orientations at that end of the billet.

Although variations in strength and Weibull modulus can be seen which suggest that orientational anisotropy exists, this can be attributed to local inhomogeneity or possibly insufficient samples being tested. The number of samples in each trial is small (18 in orientations A and B, 12 in C), and a larger number of samples is needed to reliably model the population distribution. It is for these reasons that the graphite tested is considered not to have significant orientational anisotropy.

It should be noted that the direction of cracking in the L-shaped specimens is in the same direction as the 'B' orientation. It is a coincidence that the B orientation has the lowest mean strength in both billets and the lowest value for the Weibull modulus.

3.2. Variation of properties along length of billet in the direction perpendicular to extrusion direction

The 4-point bend specimens were manufactured from each end of each billet, see Fig. 1, and the average of the Weibull modulus and mean failure stress at each end are also given in Table 2.

The average strength value (mean σ_f) determined for the section of billet is the average failure stress taken from a particular end of a billet; for example, the average failure stress for the top of billet 1 is the average failure stress of all 48 4-point bend samples from slices 1–8 (i.e. the top) of billet 1.

In comparing through billet inhomogeneity, there are 48 samples at each end of each billet. This is a large enough number to give confidence in the properties which have been determined. It can be seen that there are small but important differences at each end of each billet suggesting that the strength does vary along the length. Samples taken from the top of billet 1 are 11.9% stronger than those taken from the bottom. Similarly, samples taken from the top of billet 2 are 5.8% stronger than those at the bottom.

3.3. Billet–billet variations

Differences in properties of the two billets are also shown in Table 2 and illustrated in Fig. 3. The overall mean failure stress for the 4-point bend specimens from the two billets is 32.43 MPa and the mean failure stress of samples of billet 2 is 7.4% higher than the mean failure stress from billet 1.

3.4. Load weighting

Although no significant orientational anisotropy can be detected in the results, there is evidence of along billet inhomogeneity and billet–billet variation. These results have been used to weight the failure loads for the L-shaped specimens to normalise the originating population. It is assumed that this weighting can be performed linearly between the ends of each billet.

The weighted load to failure for a sample from billet 1 is given by:

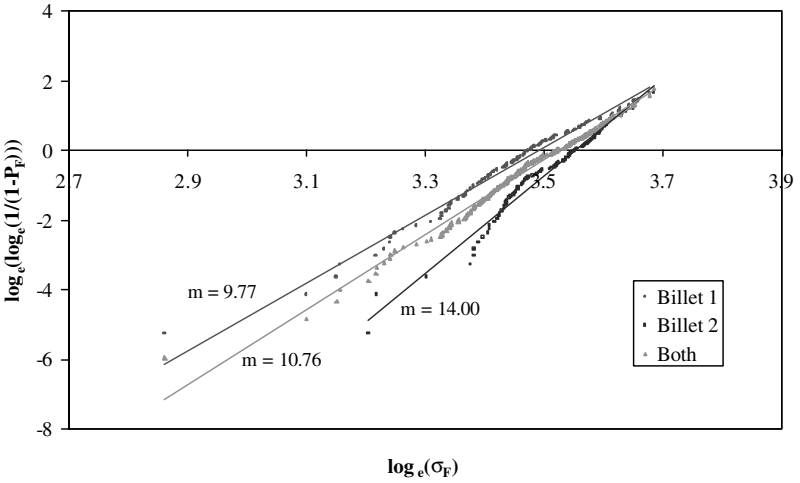

Fig. 3. Weibull plot for 4-point bend specimens from both billets.

$$L_{\mathrm{f,weighted}} = \frac{L_{\mathrm{f}}}{860}\left(\left(\frac{x}{0.9078}\right) + \left(\frac{860 - x}{1.0157}\right)\right), \quad (1)$$

where x is the distance from the centre of the top section (in mm) to the centre of the slice from which the L-shaped specimen was cut, 860 is the distance (in mm) between the centre of the top section and the centre of the bottom section, and L_{f} is the load to failure for a particular sample. Similarly, for a sample from billet 2, the weighted load to failure for a given sample is given by:

$$L_{\mathrm{f,weighted}} = \frac{L_{\mathrm{f}}}{860}\left(\left(\frac{x}{1.0088}\right) + \left(\frac{860 - x}{1.0677}\right)\right). \quad (2)$$

3.5. Effect of corner radius on Weibull modulus, failure load and strength

A summary of mean load to failure and Weibull modulus for the L-shaped specimens is given in Table 3.

The Weibull plots for the weighted loads are given in Fig. 4. The Weibull plots have been produced using load, rather than stress, to failure. This is because the stress at a sharp corner under any loading is infinite, and thus using the load to failure provides the best method of comparing different sample geometries. Since load and stress are proportionally related for a particular geometry, the Weibull modulus, m, is the same whether stress or load to failure is used.

As can be seen from Table 3 and Fig. 4, the samples with a sharp corner have a high Weibull modulus, and also fail at a lower load than samples with a larger corner radii. For the other radii m is much less but there is not a clear relationship with the corner radius r. It should be noted that the specimens with $r = 2$ mm were taken from billet 1, which has a lower m (Table 2), whereas the specimens with other corner radii were taken from billet 2.

All the specimens were measured and the moment arm calculated. Whilst there were differences between nominal (defined by sample design) and actual (found by measuring samples) moment distance between the loading point and corner these were small as can be seen in Table 4. Thus the analysis of the L-shaped specimens was performed using the nominal values.

3.6. Effect on Weibull modulus and failure load and strength of varying thickness

The effect of varying the sample thickness is described in Table 5. All of the samples tested for this effect were L-shaped specimens and had a corner radius of 2 mm, and were machined from billet 1.

Table 3
Summary of principal values for L-shaped specimens with varying corner radius when $t = 15$ mm

r (mm)	Non-weighted		Weighted	
	Weibull modulus, m	L_{mean} (N)	Weibull modulus, m	L_{mean} (N)
0	59.24	424.23	54.35	402.14
1	29.08	555.66	29.02	535.62
2	21.18	534.01	20.98	551.89
4	26.04	615.53	25.81	603.21

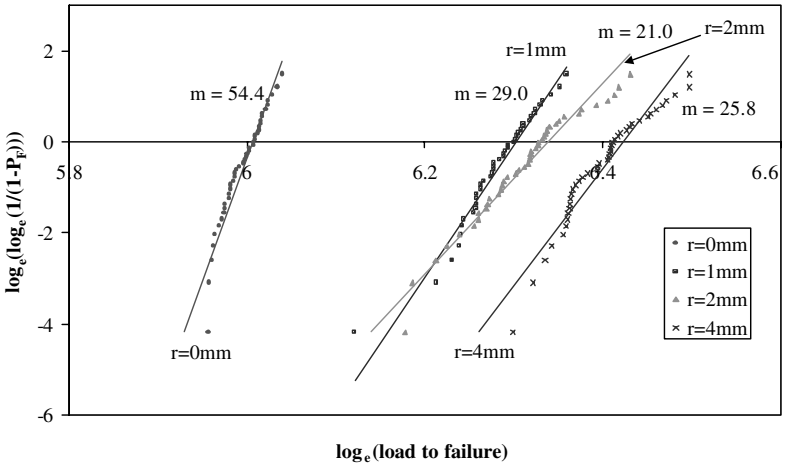

Fig. 4. Weibull plot showing comparison of different corner radii using weighted failure loads – L-shaped specimens, $t = 15$ mm.

Table 4
Moment distance (mm) between line of loading and corner radius

r (mm)	Nominal	Mean
0	23.33	23.43
1	22.92	22.98
2	22.51	22.50
4	21.68	21.72

Table 5 shows that as the sample thickness increases, the non-weighted load to failure per unit width decreases. This is expected, since with larger samples, the probability of a critical flaw existing is larger; however, the weighted loads to failure do not follow the same trend. The samples with smallest thickness also show the smallest Weibull modulus. However in the other two cases the two-parameter Weibull moduli are very similar, as can also be seen in Fig. 5. There is very little change in the mean failure load per unit thickness.

3.7. Failure mode

It can be seen from footage obtained from the high speed camera that the failure of 4-point bend specimens occurs very rapidly, and the time from onset of cracking to complete failure is very short (≈150 μs). It was clear to within a frame when the crack started to grow and when it was complete. As the cracking initiated there was a sudden and complete loss of load.

However, the mode of failure is very different for the L-shaped specimens with the load decreasing more slowly as the crosshead continued to move (see Fig. 6). For the these specimens, the crack started on the radiused face, generally near the centre, and then extended across the face. The time from visible onset of cracking to the time when the crack extends across the face of the specimen varied according to the particular geometry and it is not possible to give accurate times, as it was difficult to observe the crack opening. Whilst the cracks can be seen to open, distinguishing exactly when they open is very subjective. But the cracks can be seen and it can be seen that cracks start at different places and that these cracks then join to form a single crack which then extends across the crack face.

4. Theory

4.1. Finite element analysis of L-shaped specimens

In order to determine stresses in the L-shaped samples, the finite element software ABAQUS has been used. The specimens have been modelled in 2- and 3-D

Table 5
Summary of principal values in examining the effect of a varying specimen thickness for $r = 2$ mm

t (mm)	Non-weighted		Weighted	
	Weibull modulus, m	L_{mean} (N)/unit width	Weibull modulus, m	L_{mean} (N)/unit width
10	16.27	36.13	17.06	36.27
15	21.18	35.60	20.98	36.79
20	19.84	33.89	19.65	36.35

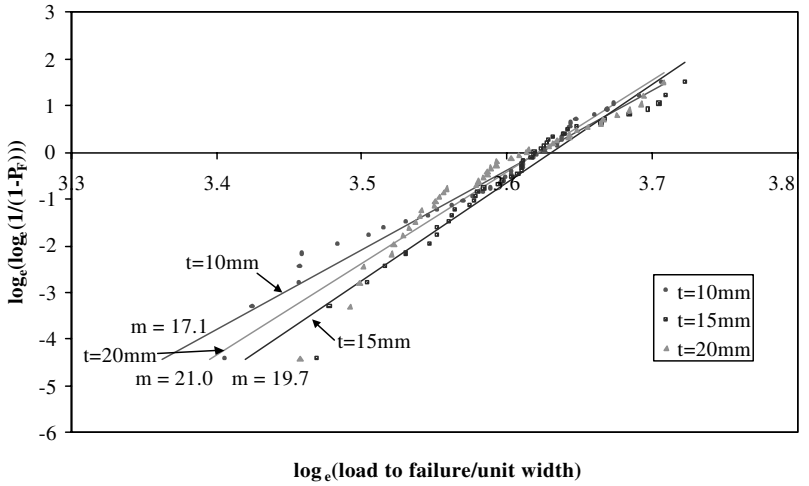

Fig. 5. Comparison of different sample thickness Weibull plots using weighted failure loads, L-shaped specimens, $r = 2$ mm.

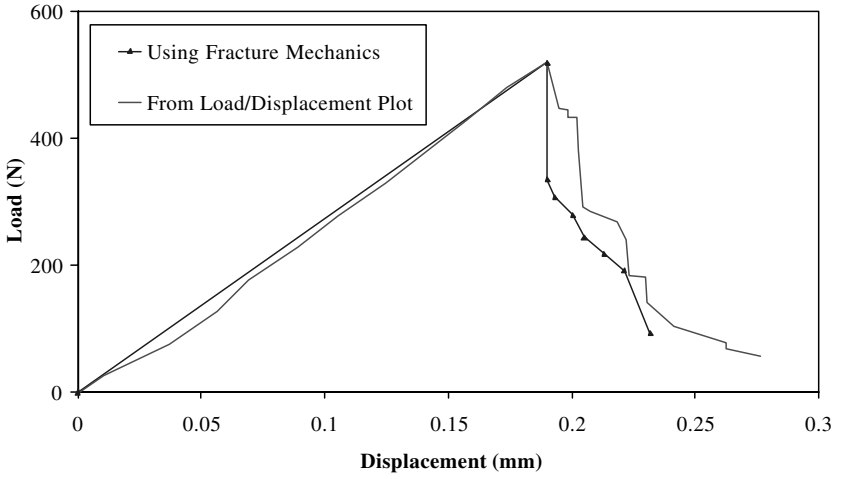

Fig. 6. Comparison of prediction using fracture mechanics and points taken from load/displacement plot.

and a 3-D model is shown in Fig. 7. Because of symmetry, in 2-D only half of the model needs to be analysed and in 3-D only a quarter of the specimen. Eight- and twenty-noded quadratic elements were used in 2- and 3-D modelling, respectively.

As the loading point is well away from the point of fracture it was decided to invoke St. Venant's principle and not model the loading in detail. Consequently, as can be seen in Fig. 7 the loading hole has not been modelled, and the pin loading which was applied to the graphite samples has been represented by a displacement applied to points along a line on a face of the model.

In order to validate the mesh, a mesh convergence study was performed in 2-D for the L-shaped specimens with corner radii of 1, 2 and 4 mm. In 2-D this meant dividing each element into 2×2 and then 3×3 elements increasing the number of elements by factors of 4 and 9. Because the loading was applied at a point, this can lead to small local perturbations around the loading point. But, when the variation in the maximum stress at the corner radius was examined, it was found that the variation in the stress per unit load applied had a maximum variation of 0.17%. With the scatter in the experimental failure loads, this is a very small effect and the mesh shown in Fig. 7 is considered to give satisfactory results.

4.2. Fracture mechanics

Cracks of different lengths were modelled, again using ABAQUS, for a 4-point bend specimen and all configurations of L-shaped specimens.

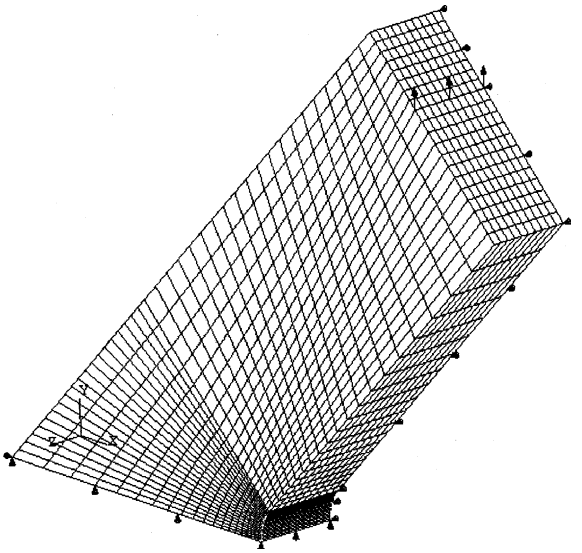

Fig. 7. 3-D FEA model of L-shaped sample ($r = 4$ mm) showing loading and boundary conditions.

Around the crack tip, nodes have been shifted to the quarter points because of the localised high stress value [5] and the crack opening displacements along the crack face were used to calculate the stress intensity factor around the crack tip (where r is the distance from the crack tip and v the opening displacement) by using [6]

$$K_{\mathrm{I}} = \frac{v}{\sqrt{r}} \frac{E\sqrt{2\pi}}{4(1-\nu^2)} \tag{3}$$

for plane strain and

$$K_{\mathrm{I}} = \frac{v}{\sqrt{r}} \frac{E\sqrt{2\pi}}{4} \tag{4}$$

for plane stress.

4.3. Britpost

The results from a finite element analysis can be used by a post-processing program BRITPOST, developed by Smart and Fok [7], which evaluates the theoretical probabilities of failure for brittle materials in 2-D or 3-D using Weibull's theory [8,9]. In this program, three different failure theories have been programmed. These are the principle of independent action (PIA), Weibull's normal stress averaging (NSA), or Evans' multiaxial elemental strength (MSE). The program is capable of integrating over the surface or volume of the model.

All three theories gave similar predictions and so only the PIA results are reported in this paper. According to the PIA [10] material subjected to a stress field must survive the effect of each of the three principal stresses, as if each acts independently. For a three dimensional stress field:

$$P_{\mathrm{s}} = P_{\mathrm{s}}(\sigma_1)P_{\mathrm{s}}(\sigma_2)P_{\mathrm{s}}(\sigma_3). \tag{5}$$

The probability of failure is therefore

$$P_{\mathrm{f}} = 1 - \exp\left\{ -\int_V \left[\left(\frac{\sigma_1}{\sigma_0}\right)^m + \left(\frac{\sigma_2}{\sigma_0}\right)^m + \left(\frac{\sigma_3}{\sigma_0}\right)^m \right] \frac{\mathrm{d}V}{v} \right\}, \tag{6}$$

which can be modified to

$$P_{\mathrm{f}} = 1 - \exp\left\{ -\left[\Gamma^m \left(1 + \frac{1}{m}\right) \left(\frac{\sigma_{\mathrm{nom}}}{\bar{\sigma}_{\mathrm{f}v}}\right)^m \frac{V}{v} \Sigma \right] \right\}, \tag{7}$$

where

$$\Sigma = \int_V \left\{ \left[\frac{\sigma_1}{\sigma_{\mathrm{nom}} H(\sigma_1)} \right]^m + \left[\frac{\sigma_2}{\sigma_{\mathrm{nom}} H(\sigma_2)} \right]^m + \left[\frac{\sigma_3}{\sigma_{\mathrm{nom}} H(\sigma_3)} \right]^m \right\} \frac{\mathrm{d}V}{V}, \tag{8}$$

Γ is the standard gamma function; σ_{nom} is a nominal stress, usually the maximum tensile stress in the component; $H(\sigma) = 1$ for tensile stresses, $H(\sigma) = -\alpha$ for compressive stresses, where α is the ratio of compressive strength to tensile strength; $\bar{\sigma}_{\mathrm{f}v}$ is the mean uniaxial failure stress per unit volume, which is related to σ_0 by $\bar{\sigma}_{\mathrm{f}v} = \Gamma\left(1 + \frac{1}{m}\right)\sigma_0$; V is the volume of the component.

Fuller information on the other theories can be found in [11].

5. Results

5.1. Stresses in L-shaped specimens

Both 2- and 3-D finite element stress analyses were performed to examine the stresses in the L-shaped specimens and the results are shown in Fig. 8. The effect of the triaxiality constraint in the specimens can be seen, particularly for the specimen with a 1 mm radius. In all cases the stresses at the centre from the 3-D analyses are close to the plane strain results. As this is where the cracks initiated, the stresses quoted for the L-shaped specimens are the 2-D plane strain results, Table 6. The value of L_{mean} is the mean load at failure for a given geometry and σ_{mean} is the value of stress calculated using the mean load for that geometry. It can be seen that the stress to failure decreases with increasing corner radius and that the maximum stress is not a good indicator of fracture as the stress varies from 67.65 to 40.02 MPa as the corner radius varies from 1 to 4 mm. These values can be compared with those from the 4-point bend tests which gave a mean stress for failure of 32.43 MPa. This could be thought of as a specimen with an infinite

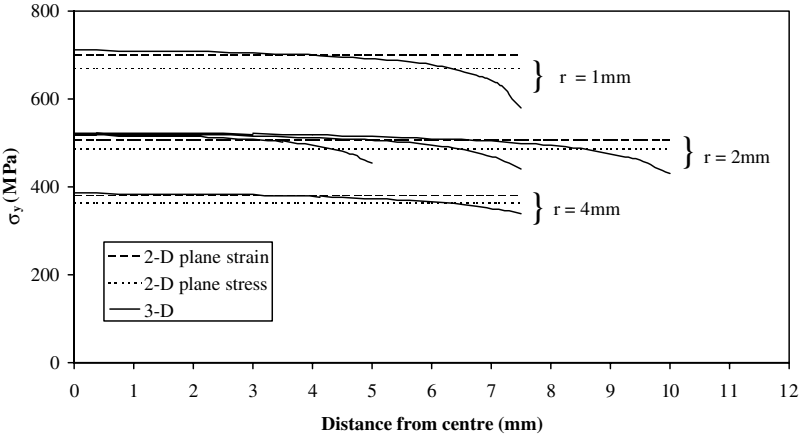

Fig. 8. Variation in σ_y (where y is the loading direction) for L-shaped specimens along centre of specimen and in the thickness direction for an applied displacement of 1 mm at the loading point.

Table 6
Summary of principal values for L-shaped specimens when $t = 15$ mm

r (mm)	Non-weighted			Weighted		
	Weibull mod, m_{2p}	L_{mean} (N)	σ_{mean} (MPa)	Weibull mod, m_{2p}	L_{mean} (N)	σ_{mean} (MPa)
0	59.24	424.23	N/A	54.35	402.14	N/A
1	29.08	555.66	70.18	29.02	535.62	67.65
2	21.18	534.01	49.74	20.98	551.89	51.41
4	26.04	615.53	40.84	25.81	603.21	40.02

radius, further confirming the decrease in failure stress with radius. For a sharp corner, the theoretical value for the stress in a linear analysis is infinite and hence there is no value for this radius in the table.

5.2. Fracture mechanics analysis

As mentioned earlier, to determine the stress intensity factor, K_I, for a crack in a specimen, 2-D plane strain elements were used with the nodes adjacent to the crack tip moved to the quarter point. The value for K_I has been determined from the nodal displacements along the crack front.

In order to compare differing corner radii, K_I is plotted against 'equivalent' crack length. Equivalent crack length is described in Fig. 9 and is the distance from the tip of the crack to the centre of the corner face of the largest radius ($r = 4$ mm). For example, a 'real' crack length of 1 mm in a sample of $r = 2$ mm corresponds to an equivalent crack length of 1.83 mm. Equivalent crack length has been used because, as the crack length increases, it is expected that the results should converge as the initial geometry becomes unimportant. That this happens is confirmed in Fig. 10 although not for the sharp corner ($r = 0$). This suggests that fracture mechanics could be used to correlate the results although not for the sharp corner. The small variations occur because of the scatter in the material properties and the consequent variation in the mean

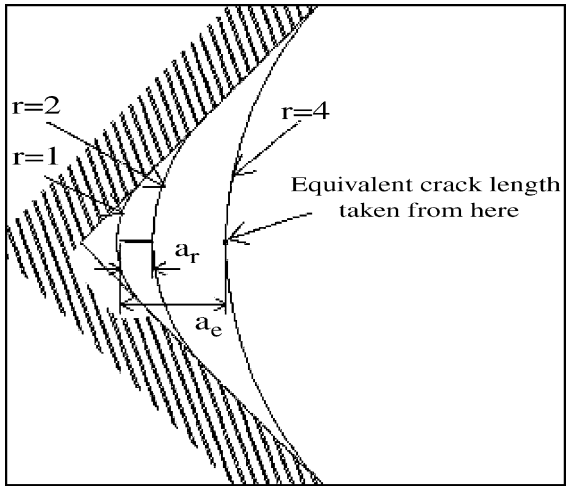

Fig. 9. Description of equivalent crack length. For $r = 2$ mm the real crack length is a_r and the equivalent crack length is a_e.

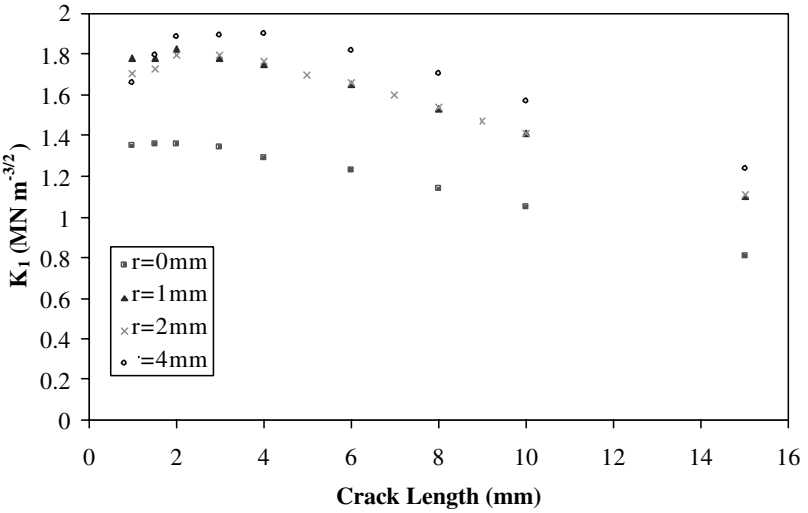

Fig. 10. Variation of stress intensity factor, K_I with equivalent crack length for an L-shaped specimen for average weighted load to failure for a given load point displacement.

failure load to failure. The shortest crack modelled had a crack length of 1.0 mm.

For the 4-point bend specimens, the variation in K_I with equivalent crack length is shown in Fig. 11.

For the L-shaped specimens, except for the specimens with a sharp corner, the value for K_I initially rises and then decreases as the crack extends. For the specimens with a 4 mm corner radius, the maximum value of K_I is 1.9 MN m$^{-3/2}$. If the curve is extrapolated back to a theoretical crack of zero length then this gives a value of about 1.6 MN m$^{-3/2}$. This is a difference of 19%. The difference is less for the other geometries. For the specimens with the sharp corner, there is a very small increase in K_I as the crack grows but the value then decreases.

However, for the 4-point bend specimens, again an initial value for a zero length crack is approximately 1.6 MN m$^{-3/2}$ but this increases to a value higher than 4.0 MN m$^{-3/2}$.

This pattern of results helps to explain the failure modes. If the fracture toughness of the graphite, K_{IC}, is assumed to be 1.6 MN m$^{-3/2}$ then once the crack has initiated in the 4-point bend specimens K_I is always higher and so the crack propagates until failure. But, for the L-shaped specimens when the equivalent crack length is about 8 mm, the value of K_I is below the fracture toughness and so further crosshead displacement is necessary for the crack to propagate further assuming that the value of K_I is the same for initiation and arrest.

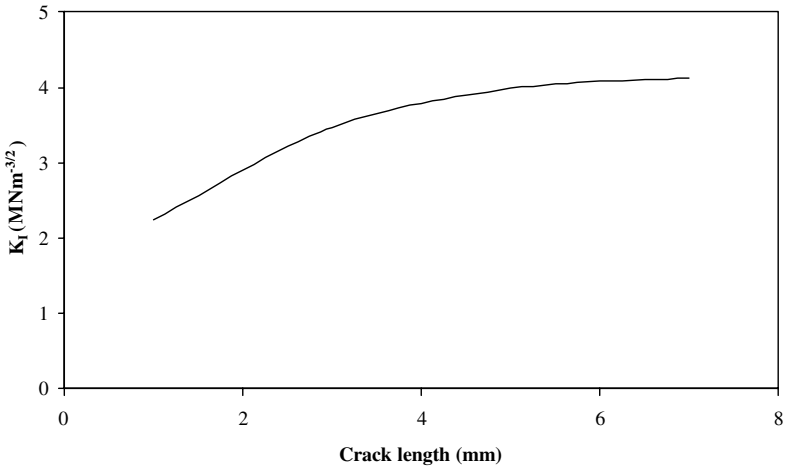

Fig. 11. Variation of K_I with increasing crack length for a 4-point bend specimen for a given load point displacement.

Hence, it is postulated that when K_I reaches a critical value, K_{IC}, the crack in the L-shaped specimen propagates to a length at which K_I is not sufficient to extend the crack further. Subsequent crosshead displacement is then necessary to extend the crack. For example, a sample of $r = 2$ is loaded until K_I is equal to approximately 1.6 MN m$^{-3/2}$ (a hypothesised K_{IC}, see Fig. 10). The crack then propagates to an equivalent length of approximately 8 mm. Additional displacement of the crosshead is then required to propagate the crack further.

For each value of K_I deduced for a particular crack length, the reaction force and applied displacement at the loading point were noted. The results were scaled so that $K_I = K_{IC}$ and the reaction force and crosshead displacement needed for the crack to extend were determined. This enables a prediction to be made of the load/displacement plot post-failure, and this is shown in Fig. 6 together with the experimental plot. It can be seen that fracture mechanics enables a reasonable prediction of the load/displacement plot post-failure to be made, but there are discrepancies. These discrepancies may be due to factors not considered such as: the variability of material properties through the sample cross-section, pop-in because of the change from plane strain to plane stress, dynamic effects, complex crack profile, sticking and friction in the apparatus, the simplistic 2-D modelling and that the crack arrests at a value different from K_{IC}. Nevertheless, the correlation is very good.

These results also help understand the results from the high speed camera. Because the value for K_I increases in the 4-point bend specimens as the crack extends the cracks fail quickly in about 150 μs.

For the L-shaped specimens it is very difficult to see the crack opening when 'looking in' at the crack face on the radius. Whilst the crack can be seen, the initiation point is difficult to identify. Nevertheless, it is clear that the crack propagates much more quickly for the specimens with a 4 mm radius compared to the other specimens. This is not surprising as Fig. 10 shows that as the corner radius decreases the increase in K_I from its initial value is also smaller. Thus, for the larger corner radius there is a greater change in K_I which causes the crack to propagate more quickly.

However, these results also show that it is probable that K_I is not a complete indicator of fracture. It can be seen very clearly that for the sharp corner the value for K_{IC} is probably about 1.3 MN m$^{-3/2}$ whereas for the larger radii is greater.

5.3. Weibull analysis

The results from using BRITPOST can be seen in Fig. 12 when using a Weibull modulus, m, of 10.76 and $\bar{\sigma}_{fv}$ of 52.24 MPa using the PIA 2-parameter model, values obtained from using the values from the 4-point bend tests. Perhaps it should be stated here that because of the variation in properties along each billet and also from billet to billet, this means that the variation in the failure stresses is higher than is probably justified leading to a lower value of m. However, the results in Fig. 12 indicate that Weibull's theory is not predicting the failure stresses. As m is probably lower than it should be, this means that the predictions for 1% and 99% probability of failure (P_f) should be closer together which would give a better fit to the experimental data. However, the trend in the mean failure stress is for the predicted values to increase more than the experimental failure values.

Weibull's NSA and Evans' MSE model have also been used to predict failure loads, and found to produce very similar predictions to the PIA model. It should be

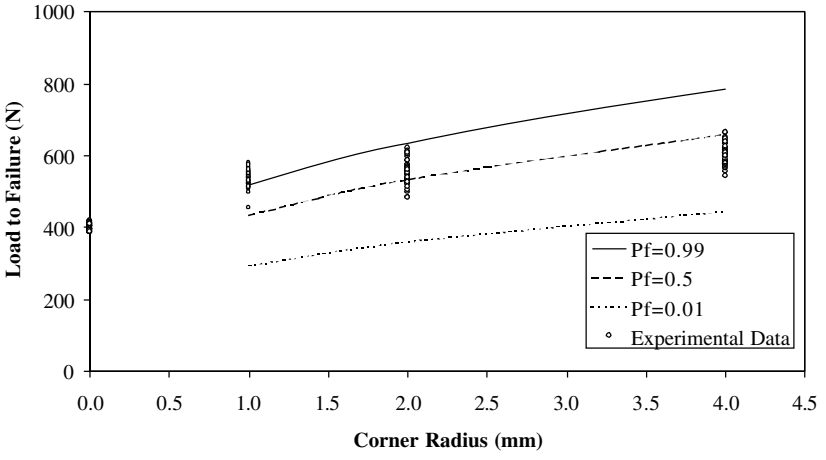

Fig. 12. Comparison of predicted failure loads using BRITPOST and actual observed weighted values – varying radius ($t = 15$ mm), PIA model.

noted that the stress field is almost uniaxial and so this is expected.

Another reason why the results may not correlate fully is that in the manufacture of the L-shaped specimens, those with a sharp corner ($r = 0$) were manufactured differently from those with a non-zero corner radius. This will mean that the finish in the corners will be different.

6. Concluding remarks

Within a billet of PPEA graphite the tests have shown that on unirradiated graphite, there is considerable inhomogeneity and also the properties vary from billet to billet. This means that extensive testing will be necessary to have confidence that the correct property values have been obtained. If the Weibull theory is to be used for an irradiated and oxidised graphite an understanding of how the Weibull parameters change with irradiation and oxidation will also be necessary.

The results have also shown that once a crack initiates then it does not necessarily propagate to failure immediately. The time it takes a crack in a 4-point bend specimen to propagate has also been found (about 150 μs) and this will provide information to allow predictions of the speed of crack growth.

An analysis has also been able to show that fracture mechanics is able to explain why the 4-point bend specimens failed immediately but the L-shaped specimens needed further crosshead movement before final failure. Good agreement has also been obtained between an experimental and predicted load displacement plot.

However, the Weibull analysis of the data has not provided a good correlation. Possibly this is because values for the Weibull parameters have been used which are found from an analysis of the total data set. This will give a low value for the Weibull modulus as the average will take into account the variation both in a billet and between billets. If a higher value had been used for the Weibull modulus, this would have given a more restricted range of predicted failure stresses.

Acknowledgements

One of the authors (B.C.M.) would like to thank the Health and Safety Executive and the EPSRC for financial support. The views expressed in this paper are those of the authors and do not necessarily represent the views of the Health and Safety Executive.

The authors would also like to acknowledge the loan of the high speed camera from EPSRC, the support of Serco Assurance (formerly AEA Technology) and the supply of the graphite by UCAR/GrafTech.

References

[1] J.E. Brocklehurst, Chem. Phys. Carbon 13 (1977) 145.
[2] J. Smart, B.C. Mitchell, S.L. Fok, B.J. Marsden, Eng. Fract. Mech. 70 (2003) 2559.
[3] J. Smart, Res. Mechanica 31 (1990) 329.
[4] S.L. Fok, J. Smart, Probabilist. Eng. Mech. 8 (1993) 67.
[5] O.C. Zienkiewicz, R.L. Taylor, in: The Finite Element Method, fifth Ed., vol. 1, McGraw Hill, London, 2000.
[6] H.L. Ewalds, R.J.H Wanhill, Fracture Mechanics, Edward Arnold, London, 1984.
[7] J. Smart, S.L. Fok, in: C.R. Brinkman, S.F. Duffy (Eds.), ASTM STP 1201, 1994, p. 143.
[8] W. Weibull, Proc. R. Swedish Inst. Eng. Res. 151 (1939) 1.
[9] A. De S. Jayatilaka, Fracture of Engineering Brittle Materials, Applied Science, London, 1979.
[10] P. Stanley, H. Fessler, A.D. Sivill, Proc. Br. Ceram. Soc. 22 (1973) 453.
[11] L. Dortmans, Th. Thiemeier, A. Bruckner-Foit, J. Smart, J. Eur. Ceram. Soc. 11 (1993) 17.